

# Complex Resonance and Radiation of Hemispherical Dielectric-Resonator Antenna with a Concentric Conductor

Kwok Wa Leung, *Member, IEEE*

**Abstract**—The probe-fed hemispherical dielectric-resonator antenna (DRA) with a concentric conductor is studied theoretically in this paper. Using the mode-matching method, the exact Green's functions for evaluation of the input impedance and radiation patterns are found, with the functions presented in computationally efficient forms. The moment method is used to determine the probe current and, hence, the input impedance as well as the radiation patterns. The results are verified by special cases available in the literature. In this paper, the effects of the conductor radius, dielectric constant, probe length, and probe displacement on the input impedance are investigated. The theory is very general and, by taking appropriate limits, can be used to study the solid DRA and the conductor-loaded wire antenna. To aid the DRA design engineer, the  $TE_{111}$ -mode characteristic equation of the DRA is also studied, from which the simple formulas for the resonant frequency and  $Q$ -factor are obtained.

**Index Terms**—Dielectric antennas, mode-matching methods, moment methods, resonance.

## I. INTRODUCTION

SINCE the work reported by Long *et al.* [1], the dielectric-resonator antenna (DRA) has been studied extensively [2]–[11]. The DRA offers a number of advantages such as its small size and low cost. Moreover, as compared with the microstrip antenna, the DRA has a much wider bandwidth ( $\sim 10\%$  for dielectric constant  $\epsilon_r \sim 10$ ).

Among various shapes of the DRA, the hemispherical one has the simplest structure for the analytical analysis [6], [7]. Recently, an air gap has been introduced to the hemispherical DRA to increase the antenna bandwidth [8]. Replacing the air gap with a concentric conductor is of interest [9]. In this paper, the broadside  $TE_{111}$  mode of a probe-fed hemispherical DRA with a concentric conductor (Fig. 1) is studied theoretically, and the results are verified by the limiting cases available in the literature. Similar to the previous air-gap DRA, the new structure provides a wider bandwidth and a higher resonant frequency than the solid one. As will be shown later, the new structure provides even a wider frequency range than the air-gap version. Although a wider bandwidth with a higher resonant frequency can also be achieved by using materials of lower dielectric constant, the new structure does provide an alternative for the DRA design engineer. The present theory is more general than the previous one [6], [7], as the latter can be obtained from the former by reducing the conductor radius to zero. Moreover, by taking

the limit of  $\epsilon_r \rightarrow 1$  the present theory is reduced to the solution of a wire in the presence of a conducting sphere [12], [13], which is useful to the electromagnetic compatibility (EMC) engineer. Practically, to avoid any possible air gaps between the conductor and DRA, the inner DRA surface can be coated with a conducting material, e.g., silver epoxy or adhesive conducting tape. Since the embedding solid conductor is, in fact, unnecessary, the present DRA can be easily obtained from an air-gap DRA. It should be mentioned that as DRAs of different shapes show a very similar behavior, the characteristics of others (e.g., rectangular and cylindrical DRAs) can be anticipated from the knowledge of the hemispherical version.

In this paper, the mode-matching method [6] is used to derive the characteristic equation and exact antenna Green's function of the DRA. From the former, the source-free resonant frequency and  $Q$ -factor can be determined. To aid the engineer in designing the DRA, two simple curve-fitting formulas are given so that the resonant frequency and  $Q$ -factor can be determined quickly and easily. The effects of the dielectric constant  $\epsilon_r$  and conductor radius on the complex resonant frequency are studied, and the results are compared with those of the solid dielectric sphere [14] and of the air-gap DRA. In this paper, the radiation characteristics of the DRA are also investigated. The Green's function technique and the moment method (MoM) are used to find the probe current and, hence, the input impedance. The results are compared with those of the previous solid-DRA case [6]. The effects of the conductor radius, dielectric constant, probe length, and probe displacement on the input impedance are studied. In addition, the expressions of the radiation fields are presented. The solution takes all higher order modes into account and, thus, can be used to calculate the cross-polarized fields. As the rigorous far-field expressions have not been reported explicitly in the literature [6], [7] even for the solid DRA case, the results are very useful for the DRA design engineer.

In Section II, the formulation of the problem using the mode-matching method is presented. The results of the complex resonant frequency, input impedance, and radiation patterns will be given in Section III. Section IV concludes the study.

## II. THEORY

The antenna configuration is shown in Fig. 1, where the DRA of outer radius  $a$  and inner radius  $c$  is fed by a probe of length  $l$ , displacement  $b$ , and radius  $r_1$ . The outer radius of the coaxial aperture is  $r_2$ . In the following formulation, the fields are assumed to vary harmonically as  $e^{j\omega t}$ , which is suppressed throughout. The field and source points are denoted by  $\vec{r}(r, \theta, \phi)$

Manuscript received May 22, 1998.

The author is with the Department of Electronic Engineering, City University of Hong Kong, Kowloon, Hong Kong (e-mail: eekleung@cityu.edu.hk).

Publisher Item Identifier S 0018-9480(01)01688-X.

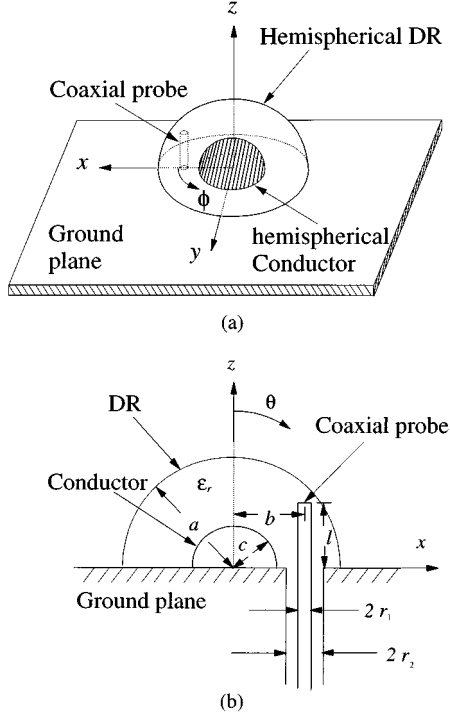


Fig. 1. Configuration of the hemispherical DRA with a concentric conductor. (a) Perspective view. (b) Side view.

and  $\vec{r}'(r', \theta', \phi')$ , respectively. To begin with, image theory is invoked to remove the ground plane, and the equivalence principle is used to replace the coaxial aperture by an equivalent magnetic frill current. The equivalent problem is a dipole embedded inside a dielectric sphere with a concentric spherical conductor. To tackle the problem, the  $\hat{z}$ -directed current is first resolved into the  $\theta$ - and  $r$ -directed components. The potential Green's functions of the components are then found separately. To enhance the computational efficiency, the Green's function are divided into their particular and homogeneous parts [6]. Since there are two boundaries (DR–air and DR–conductor interfaces) to be matched, two spherical Bessel functions are required inside the dielectric ( $c \leq r \leq a$ ) for the homogeneous solutions. After the potential Green's functions are obtained, the various  $E$ - and  $H$ -field Green's functions can be obtained easily.

Using the MoM, the probe current  $I(z)$  is expanded by a set of basis functions  $f_n(z)$  as follows:

$$I(z) = \sum_{n=1}^N I_n f_n(z). \quad (1)$$

In this paper, the piecewise sinusoidal (PWS) functions are used for  $f_n(z)$  [6]. The Green's function of  $E_z$  due to a  $z$ -directed point current is denoted by  $G_{J_z}^{E_z} = G_P + G_H$ , where the subscripts  $P$  and  $H$  stand for the particular and homogeneous solutions, respectively. The unknown coefficients  $I_n$ 's are then solved via the following matrix equation:

$$[Z_{mn}^P + Z_{mn}^H] [I_n] = [V_m] \quad (2)$$

where

$$Z_{mn}^{P,H} = \iint_{S_0} \iint_{S_0'} f_m(z) G_{P,H} f_n(z') dS' dS \quad (3)$$

in which

$$G_P = \frac{-j}{\omega \epsilon} \left( \frac{\partial^2}{\partial z^2} + k^2 \right) \frac{e^{-jkR}}{4\pi R} \quad (4a)$$

$$\begin{aligned} G_H = & \frac{-1}{4\pi\omega\epsilon k} \cdot \frac{\cos\theta' \cos\theta}{r^2 r'^2} \sum_{n=1}^{\infty} n(n+1)(2n+1) P_n(\cos\xi) \\ & \cdot \left[ j_n \hat{J}_n(kr) + k_n \hat{H}_n^{(2)}(kr) \right] \\ & + \frac{1}{4\pi\omega\epsilon} \cdot \frac{\sin\theta' \cos\theta}{r^2 r'} \sum_{n=1}^{\infty} (2n+1) \frac{\partial}{\partial\theta'} P_n(\cos\xi) \\ & \cdot \left[ e_n \hat{J}_n(kr) + f_n \hat{H}_n^{(2)}(kr) \right] \\ & + \frac{1}{4\pi\omega\epsilon} \cdot \frac{\cos\theta' \sin\theta}{r r'^2} \sum_{n=1}^{\infty} (2n+1) \frac{\partial}{\partial\theta} P_n(\cos\xi) \\ & \cdot \left[ j_n \hat{J}'_n(kr) + k_n \hat{H}'_n^{(2)}(kr) \right] \\ & - \frac{k}{4\pi\omega\epsilon} \cdot \frac{1}{r r'} \sum_{n=1}^{\infty} \frac{2n+1}{n(n+1)} \frac{\partial^2}{\partial\phi\partial\phi'} P_n(\cos\xi) \\ & \cdot \left[ b_n \hat{J}_n(kr) + c_n \hat{H}_n^{(2)}(kr) \right] \\ & - \frac{k}{4\pi\omega\epsilon} \cdot \frac{\sin\theta \sin\theta'}{r r'} \sum_{n=1}^{\infty} \frac{2n+1}{n(n+1)} \frac{\partial^2}{\partial\theta\partial\theta'} P_n(\cos\xi) \\ & \cdot \left[ e_n \hat{J}'_n(kr) + f_n \hat{H}'_n^{(2)}(kr) \right] \end{aligned} \quad (4b)$$

$$\cos\xi = \cos\theta \cos\theta' + \sin\theta \sin\theta' \cos(\phi - \phi') \quad (4c)$$

and  $R = |\vec{r} - \vec{r}'|$  is the distance between the field and source points. The various symbols were defined in [6], whereas the modal coefficients are given in Appendix A. It is interesting to observe that as  $c \rightarrow 0$ , the homogeneous solution  $G_H$  converges to that given in [6, eq. (19b)], which is to be expected. When  $\epsilon_r \rightarrow 1$ , the explicit Green's function for a wire in the presence of a spherical conductor is obtained. If, in addition,  $c \rightarrow 0$ , the homogeneous solution  $G_H$  vanishes and  $G_{J_z}^{E_z}$  is reduced to the Green's function of an electric dipole radiating in free space [see (4a)], as expected.

#### A. Input Impedance

In (4a), the slowly convergent modal series of the particular solution  $G_P$  has been replaced by a simple form to improve the computational efficiency [6]. As will be shown in Section III,  $G_H$  is a smooth function, which converges very quickly and, thus,  $Z_{mn}^H$  can be easily calculated in a straightforward manner. However, special attention is needed in evaluating  $Z_{mn}^P$  because  $G_P$  is a singular function at  $\vec{r} = \vec{r}'$ . As discussed in [6], this problem can be avoided by using the reduced kernel. When PWS current modes are used with the reduced kernel, a simple formula exists [16], which has been documented by Pozar [17]. The result is summarized as follows for completeness:

$$\begin{aligned} Z_{mn}^P = & \frac{1}{\sqrt{\epsilon_r}} \cdot \frac{15}{\sin^2 kd} \sum_{p=-2}^2 \sum_{\substack{q=-1 \\ (\text{step } 2)}}^1 A(p+3) \\ & \cdot e^{-jkq(x_0+pd)} E(k\beta) \end{aligned} \quad (5a)$$

where

$$\beta = \sqrt{r_1^2 + (x_0 + pd)^2} - q(x_0 + pd) \quad (5b)$$

$$x_0 = |m - n|d \quad (5c)$$

$$A(1) = A(5) = 1 \quad (5d)$$

$$A(2) = A(4) = -4 \cos kd \quad (5e)$$

$$A(3) = 2 + 4 \cos^2 kd \quad (5f)$$

$$E(k\beta) = \text{Ci}(k\beta) - j\text{Si}(\beta) \quad (5g)$$

and  $d = 2l/(N + 1)$  is the PWS mode half-length. In (5g),  $\text{Ci}(x)$  and  $\text{Si}(x)$  are cosine and sine integrals, respectively, and their values can be easily computed by using simple formulas [18]. Note that the factor of  $1/\sqrt{\epsilon_r}$  is added to  $Z_{mn}^P$  so that the surrounding of the dipole is a dielectric medium of permittivity  $\epsilon_r$ , instead of air, as considered in [16] and [17]. To improve the accuracy of the solution and yet retain the simplicity, the two-term equivalent radius  $r_e$  [6], [19] is used in (5a) and (5b).

The elements of the voltage vector  $[V_m]$  were discussed in [6] and are omitted here for brevity. After solving the probe current, the input impedance of the equivalent problem is obtained easily from  $Z_{\text{in}} = 1/\sum_{n=1}^N I_n f_n(0)$ . Dividing this impedance by two gives the input impedance of the original problem.

### B. Radiation Fields

By using the dyadic Green's function approach [6], it can be proven that the Green's function of  $E_\theta$  due to a  $z$ -directed point current is given by

$$G_{J_z}^{E_\theta} = G_{J_r}^{E_\theta} \cos \theta' - G_{J_\theta}^{E_\theta} \sin \theta' \quad (6)$$

and that of  $H_\theta$  by

$$G_{J_z}^{H_\theta} = G_{J_r}^{H_\theta} \cos \theta' - G_{J_\theta}^{H_\theta} \sin \theta' \quad (7)$$

where  $G_{J_r}^{E_\theta}$ ,  $G_{J_\theta}^{E_\theta}$ ,  $G_{J_r}^{H_\theta}$ , and  $G_{J_\theta}^{H_\theta}$  are obtained from the potential Green's functions. After simplification, the Green's functions  $G_{J_z}^{E_\theta}$  and  $G_{J_z}^{H_\theta}$  are obtained as follows ( $r \geq a$ ):

$$\begin{aligned} G_{J_z}^{E_\theta} &= \frac{-jk_0}{4\pi\omega\epsilon_0} \cdot \frac{1'}{rr' \sin \theta} \sum_{n=1}^{\infty} \frac{2n+1}{n(n+1)\delta_n^{\text{TE}}} \\ &\cdot \left[ \hat{J}_n(kr') - \frac{\hat{H}_n^{(2)}(kr') \hat{J}_n(kc)}{\hat{H}_n^{(2)}(kc)} \right] \\ &\cdot \frac{\partial^2 P_n(\cos \xi)}{\partial \phi \partial \phi'} \hat{H}_n^{(2)}(k_0 r) \\ &- \frac{jk_0}{4\pi\omega\epsilon_0 k} \cdot \frac{\cos \theta'}{rr'^2} \sum_{n=1}^{\infty} \frac{2n+1}{\delta_n^{\text{TM}}} \\ &\cdot \left[ \hat{J}_n(kr') - \frac{\hat{H}_n^{(2)}(kr') \hat{J}'_n(kc)}{\hat{H}_n^{(2)}(kc)} \right] \\ &\cdot \frac{\partial P_n(\cos \xi)}{\partial \theta} \hat{H}_n^{(2)}(k_0 r) \\ &+ \frac{jk_0}{4\pi\omega\epsilon_0} \cdot \frac{\sin \theta'}{rr'} \sum_{n=1}^{\infty} \frac{2n+1}{n(n+1)\delta_n^{\text{TM}}} \\ &\cdot \left[ \hat{J}'_n(kr') - \frac{\hat{H}_n^{(2)}(kr') \hat{J}'_n(kc)}{\hat{H}_n^{(2)}(kc)} \right] \\ &\cdot \frac{\partial P_n(\cos \xi)}{\partial \theta \partial \theta'} \hat{H}_n^{(2)}(k_0 r) \end{aligned} \quad (8)$$

$$\begin{aligned} G_{J_z}^{H_\theta} &= \frac{1}{4\pi} \cdot \frac{\sin \theta'}{rr'} \sum_{n=1}^{\infty} \frac{2n+1}{n(n+1)\delta_n^{\text{TE}}} \\ &\cdot \left[ \hat{J}_n(kr') - \frac{\hat{H}_n^{(2)}(kr') \hat{J}_n(kc)}{\hat{H}_n^{(2)}(kc)} \right] \\ &\cdot \frac{\partial^2 P_n(\cos \xi)}{\partial \theta \partial \phi'} \hat{H}_n^{(2)}(k_0 r) \\ &+ \frac{1}{4\pi k} \cdot \frac{\cos \theta'}{rr'^2 \sin \theta} \sum_{n=1}^{\infty} \frac{2n+1}{\delta_n^{\text{TM}}} \\ &\cdot \left[ \hat{J}_n(kr') - \frac{\hat{H}_n^{(2)}(kr') \hat{J}'_n(kc)}{\hat{H}_n^{(2)}(kc)} \right] \\ &\cdot \frac{\partial P_n(\cos \xi)}{\partial \phi} \hat{H}_n^{(2)}(k_0 r) \\ &- \frac{1}{4\pi} \cdot \frac{\sin \theta'}{rr' \sin \theta} \sum_{n=1}^{\infty} \frac{2n+1}{n(n+1)\delta_n^{\text{TM}}} \\ &\cdot \left[ \hat{J}'_n(kr') - \frac{\hat{H}_n^{(2)}(kr') \hat{J}'_n(kc)}{\hat{H}_n^{(2)}(kc)} \right] \\ &\cdot \frac{\partial^2 P_n(\cos \xi)}{\partial \phi \partial \theta'} \hat{H}_n^{(2)}(k_0 r) \end{aligned} \quad (9)$$

where  $\delta_n^{\text{TE}}$  and  $\delta_n^{\text{TM}}$  are given in Appendix A. From the Green's functions, the  $E_\theta$ - and  $H_\theta$ -fields outside the DRA are obtained as follows:

$$E_\theta(\vec{r}) = \iint_{S_0} G_{J_z}^{E_\theta}(\vec{r}, \vec{r}') J_z(z') dS' \quad (10)$$

$$H_\theta(\vec{r}) = \iint_{S_0} G_{J_z}^{H_\theta}(\vec{r}, \vec{r}') J_z(z') dS'. \quad (11)$$

In calculating the far fields, the asymptotic expressions  $\hat{H}_n^{(2)}(k_0 r) \sim j^{n+1} e^{-jk_0 r}$  and  $\hat{H}_n^{(2)}(k_0 r) \sim -j \hat{H}_n^{(2)}(k_0 r)$  are used.

### C. Complex Resonant Frequency

The complex resonant frequency for various TE modes can be obtained by solving  $\delta_n^{\text{TE}} = 0$ . In general, the solution, denoted by  $\Omega$ , is a complex number from which the source-free resonant frequency  $f_r$  and  $Q$ -factor are found as follows:

$$f_r = \frac{\omega_r}{2\pi} = \text{Re}(\Omega) \quad (12a)$$

$$Q = \frac{\text{Re}(\Omega)}{2\text{Im}(\Omega)} \quad (12b)$$

where  $\text{Re}(\cdot)$  and  $\text{Im}(\cdot)$  denote the real and imaginary parts of the argument, respectively. To easily determine the resonant frequency and  $Q$ -factor, simple formulas are obtained using the curve-fitting technique. The results are given as follows:

$$f_r (\text{GHz}) = A_1 (\sqrt{\epsilon_r} + A_2)^{-A_3}, \quad 4 \leq \epsilon_r \leq 80 \quad (13)$$

$$Q = B_1 \epsilon_r^{B_2} e^{B_3 \epsilon_r}, \quad 6 \leq \epsilon_r \leq 80 \quad (14)$$

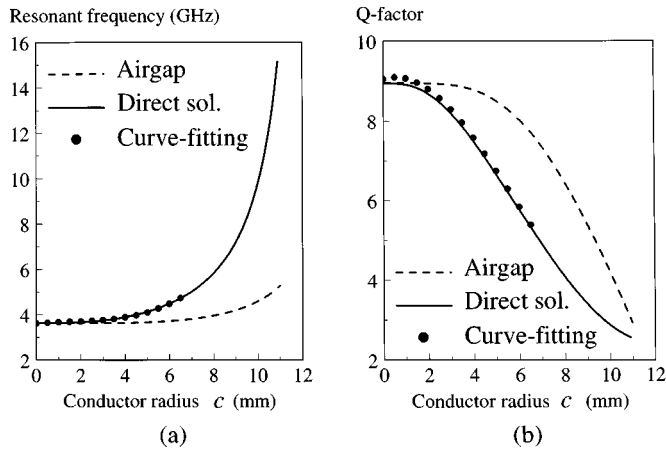


Fig. 2. Resonant frequencies and  $Q$ -factors of the present and air-gap DRAs as a function of inner radius  $c$ :  $a = 12.5$  mm and  $\epsilon_r = 9.8$ . (a) Resonant frequency. (b)  $Q$ -factor.

where

$$A_1 = \frac{30}{a(\text{mm})} \left( 4.9848 + 1.7841t - 7.319t^2 + 17.4513t^3 \right)$$

$$A_2 = 0.20261 + 0.1819t - 0.3234t^2 - 0.1792t^3$$

$$A_3 = 0.9968 + 0.005t + 0.0069t^2 - 0.1376t^3$$

$$B_1 = 0.01 \times \left( 72.5101 + 21.7658t - 180.647t^2 + 164.2913t^3 \right)$$

$$B_2 = 0.01 \times \left( 108.2226 - 4.8076t + 1.1518t^2 - 79.254t^3 \right)$$

$$B_3 = 0.01 \times \left( 0.5527 + 0.2149t - 0.8309t^2 + 1.3113t^3 \right)$$

and  $t = c/a$ , with  $0 \leq t \leq 0.6$ . Within the nominal ranges, the errors are less than 1.5% and 2.5% for  $f_r$  and  $Q$ , respectively. At  $c/a = 0.64$ , which is outside the nominal range, the maximum error of the resonant frequency is less than 2%, but that of the  $Q$ -factor becomes 3.2%. Note that the results are applicable to the solid DRA case by putting  $t = 0$ . In this paper, the results are compared with those of the air-gap DRA, whose  $\text{TE}_{1mr}$ -mode characteristic equation is given in Appendix B.

### III. RESULTS AND DISCUSSIONS

The complex resonance of the new structure is studied first. The  $\text{TE}_{111}$ -mode resonant frequency and  $Q$ -factor obtained by solving the characteristic equation  $\delta_1^{\text{TE}} = 0$  are shown in Fig. 2, where very good agreement between the direct solution and curve-fitting formulas is obtained. As can be observed from Fig. 2, the resonant frequency  $f_r$  increases with, and the  $Q$ -factor decreases with, increasing the conductor radius  $c$ . This is because increasing the conductor radius will reduce the dielectric volume, causing a higher resonant frequency and a lower stored energy. For ease of comparison, the complex frequency of the air gap version is also shown in the figure. From Fig. 2(a), it is found that the conductor case offers a wider frequency range than the air-gap counterpart. It is observed from Fig. 2(b) that the conductor case has a lower  $Q$ -factor than the air-gap version, as the electromagnetic energy can be stored in an air gap, but cannot be stored in a conductor.

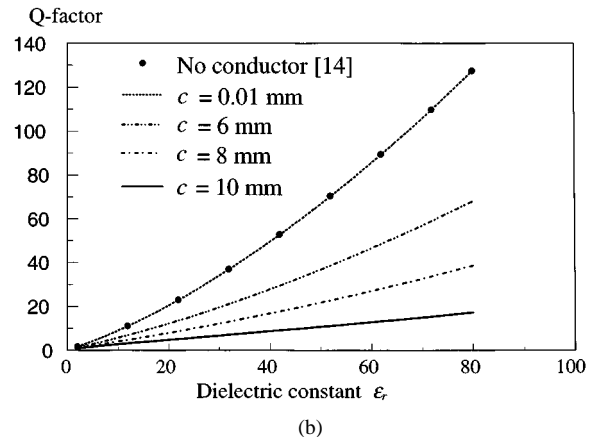
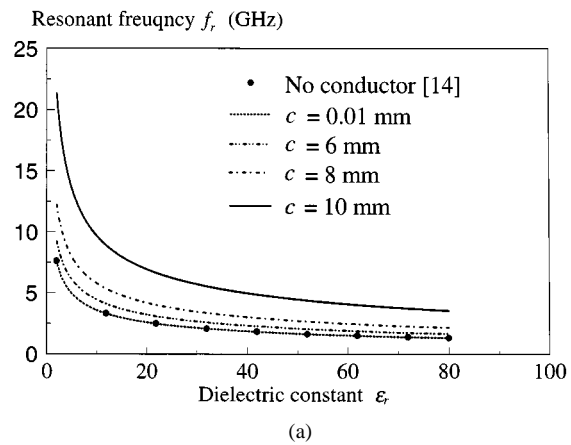


Fig. 3. Resonant frequency and  $Q$ -factor of the DRA as a function of dielectric constant  $\epsilon_r$  for  $c = 0.01, 6, 8,$  and  $10$  mm:  $a = 12.5$  mm. (a) Resonant frequency. (b)  $Q$ -factor.

Fig. 3 shows the resonant frequency and  $Q$ -factor as a function of dielectric constant  $\epsilon_r$  for  $c = 0.01, 6, 8,$  and  $10$  mm. Observe that the results of  $c \rightarrow 0$  ( $c = 0.01$  mm) agree excellently with those of the previous solution [14] and the validity of the present theory is verified. With reference to the figure, the higher the dielectric constant  $\epsilon_r$  is, the lower the resonant frequency  $f_r$  and the higher the  $Q$ -factor, as expected. The curve-fitting formulas (13) and (14) were checked and accurate results were obtained within the nominal ranges.

Fig. 4 shows the convergence check for  $G_H$ . It is seen that the real part of  $G_H$  requires only a few terms to converge, whereas the imaginary part of  $G_H$  requires about 13 terms. In this paper, 14 terms were used in the calculations. To check the validity of the MoM solution, the solution was first compared with that of [13] for  $\epsilon_r \rightarrow 1$  and excellent agreement was obtained. Next, we consider another special case of  $c \rightarrow 0$ . Fig. 5 compares the theory for  $c = 0.01$  mm with the previous solid DRA solution [6]. Again, excellent agreement between them is found. Also shown in Fig. 5 are the input impedances for  $c = 4$  and  $6$  mm. It is observed that the results of  $c = 4$  and  $6$  mm have higher resonant frequencies and wider impedance bandwidths, but their reactances shift upward due to the presence of the conductor.

Fig. 6(a)–(c) displays the radiation patterns of the DRA for  $c = 0.01, 4,$  and  $6$  mm, respectively. The field patterns were calculated at their respective resonant frequencies. With reference to Fig. 6(a) ( $c = 0.01$  mm), the  $E$ -plane field pattern is

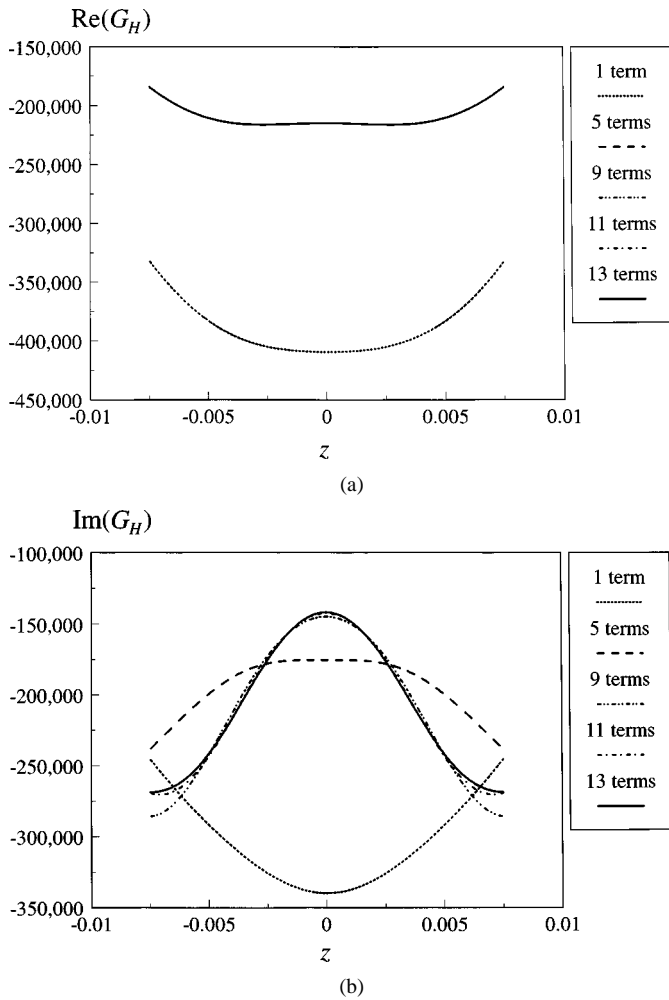


Fig. 4. Convergence check of  $G_H$ :  $a = 12.5$  mm,  $\epsilon_r = 9.8$ ,  $c = 4$  mm,  $b = 8$  mm,  $l = 7.5$  mm,  $r_1 = 0.63$  mm,  $r_2 = 2.0$  mm, and  $z' = 0$ . (a)  $\text{Re}(G_H)$  and (b)  $\text{Im}(G_H)$ .

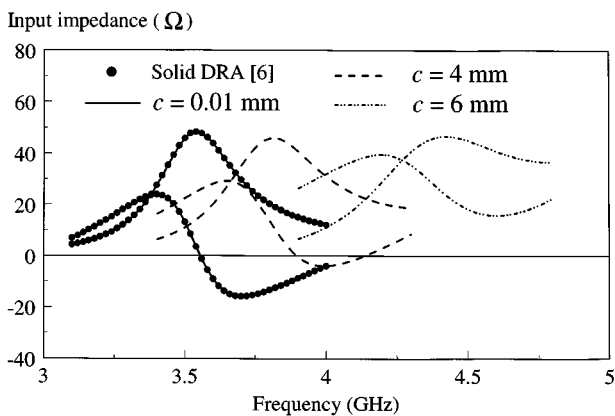


Fig. 5. Input impedance of the DRA as a function of frequency for  $c = 0.01$ , 4, and 6 mm:  $a = 12.5$  mm,  $\epsilon_r = 9.8$ ,  $b = 8$  mm,  $l = 7.5$  mm,  $r_1 = 0.63$  mm, and  $r_2 = 2.0$  mm.

nearly omnidirectional, whereas the  $H$ -plane exhibits a broadside mode. When  $c = 4$  mm [see Fig. 6(b)], the  $E$ -plane field pattern is somewhat asymmetric. The  $H$ -plane field pattern, however, remains symmetric, as expected. As  $c$  is further increased to 6 mm [see Fig. 6(c)], the asymmetry of the  $E$ -plane

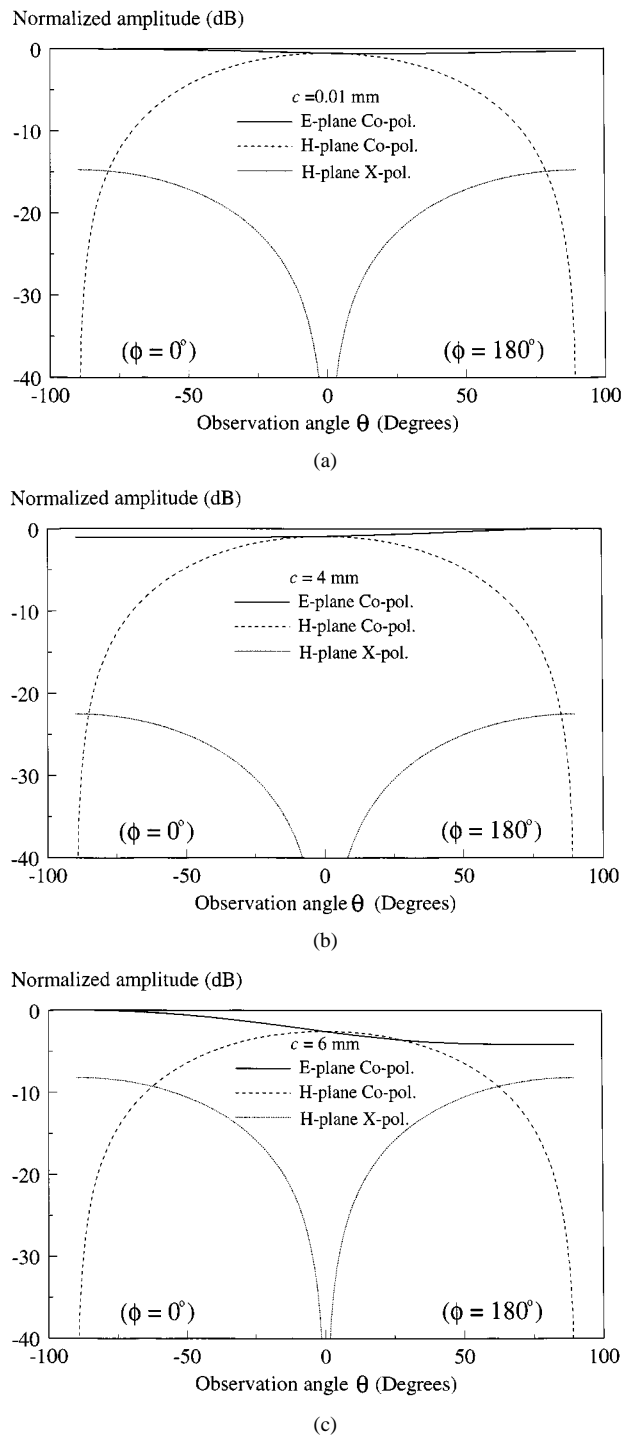


Fig. 6. Radiation patterns of the DRA. The parameters are the same as Fig. 5. (a)  $c = 0.01$  mm. (b)  $c = 4$  mm. (c)  $c = 6$  mm.

field pattern becomes even more obvious, while the  $H$ -plane field pattern still remains symmetric. From Fig. 6, it is seen that the maximum  $E$ -plane radiation field may occur on the probe side ( $\phi = 0^\circ$ ) or the opposite side ( $\phi = 180^\circ$ ). A similar phenomenon was observed in [12], though in [12], the displacement of the dipole was changed instead of the conductor radius. For ease of comparison, the  $H$ -plane cross-polarized fields are also shown in the figure (the  $E$ -plane cross-polarized fields were theoretically zero). In all the cases, the cross-polarized fields are extremely weak in the broadside direction ( $\theta = 0$ ). The level of

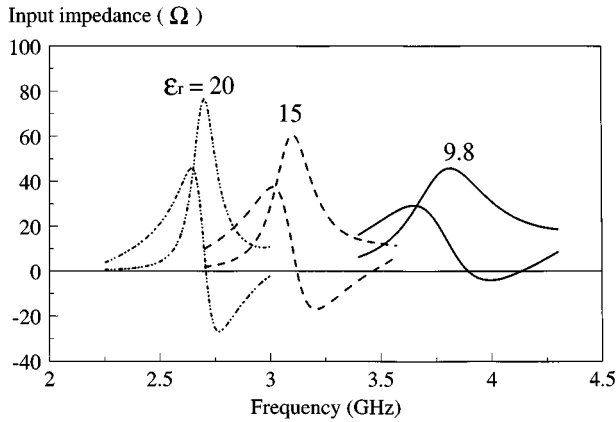


Fig. 7. Input impedance of the DRA as a function of frequency for  $\epsilon_r = 9.8$ , 15, and 20:  $a = 12.5$  mm,  $c = 4$  mm,  $b = 8$  mm,  $l = 7.5$  mm,  $r_1 = 0.63$  mm, and  $r_2 = 2.0$  mm.

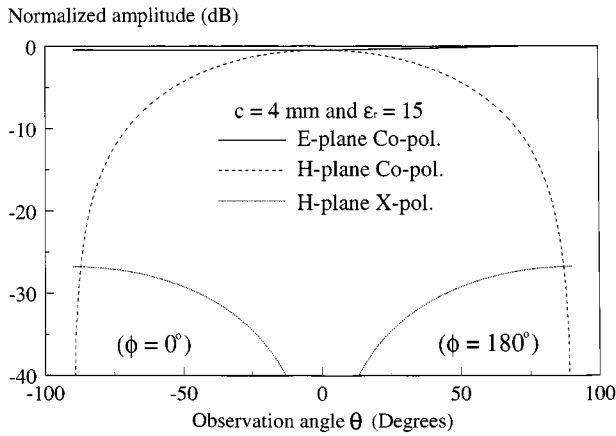


Fig. 8. Radiation patterns of the DRA for  $\epsilon_r = 15$ . Other parameters are the same as Fig. 7.

the cross-polarized fields increases with  $\theta$ , but it oscillates as  $c$  is varied.

Fig. 7 shows the input impedance of the DRA for  $\epsilon_r = 9.8$ , 15, and 20 with  $c = 4$  mm. It is seen that the higher the dielectric constant is, the lower the resonant frequency and the narrower the bandwidth, as expected. Moreover, the peak resistance increases with, and the radiated power decreases with, increasing  $\epsilon_r$ . The results are similar to those of the solid DRA [6]. With reference to the figure, using a higher  $\epsilon_r$  causes the reactance to shift downward. Fig. 8 shows the radiation patterns of the DRA for  $\epsilon_r = 15$  with  $c = 4$  mm. It is seen that the symmetry of the  $E$ -plane field pattern is restored by using a higher  $\epsilon_r$ . This is because an increase of  $\epsilon_r$  will strengthen the DR mode, resulting in the symmetric pattern. The field patterns for  $\epsilon_r = 20$  with  $c = 4$  mm were also obtained. It was found that the symmetry of the  $E$ -plane field pattern was further improved, as expected.

Fig. 9 shows the input impedance of the DRA for  $c = 4$  mm and  $l = 6.5, 7.5$ , and  $8.5$  mm. As can be observed from the figure, the input impedance increases with, and the (probe-loaded) resonant frequency slightly decreases with, increasing  $l$ . (There are two kinds of resonant frequency in this paper, namely source-free and probe-loaded. The resonant frequency found by solving  $\delta_1^{\text{TE}} = 0$  is source-free, i.e., the probe is not taken into account and the solution is, therefore,

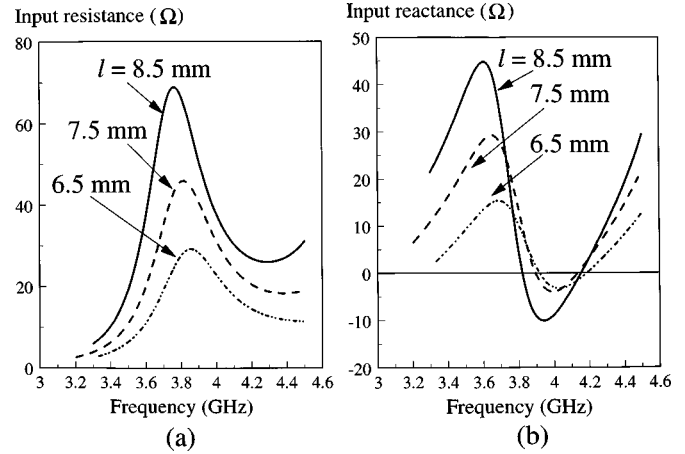


Fig. 9. Input resistance and reactance of the DRA as a function of frequency for  $l = 6.5, 7.5$ , and  $8.5$  mm:  $a = 12.5$  mm,  $c = 4$  mm,  $\epsilon_r = 9.8$ ,  $b = 8$  mm,  $r_1 = 0.63$  mm, and  $r_2 = 2.0$  mm. (a) Input resistance. (b) Input reactance.

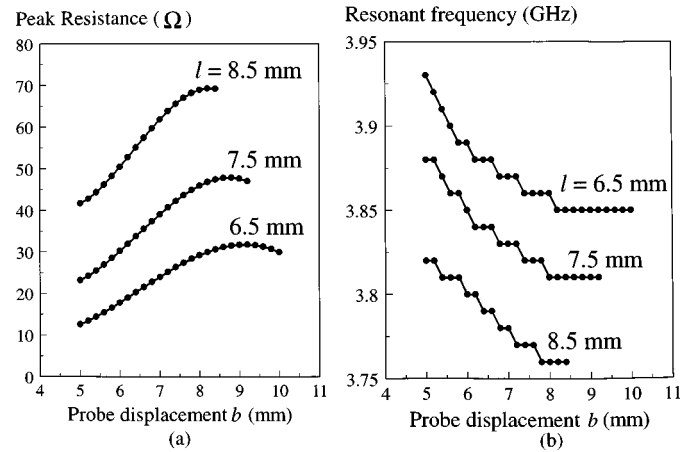


Fig. 10. Peak resistance and resonant frequency as a function of displacement  $b$  for  $l = 6.5, 7.5$ , and  $8.5$  mm:  $a = 12.5$  mm,  $c = 4$  mm,  $\epsilon_r = 9.8$ ,  $r_1 = 0.63$  mm, and  $r_2 = 2.0$  mm. (a) Peak resistance. (b) Resonant frequency.

independent of  $l$ . For the probe-loaded resonant frequency, however, the value is found at the peak resistance point, with the resistance rigorously calculated using the MoM. Thus, in this case, the result does vary with  $l$ .) The results are, again, similar to those of the solid DRA [6]. The corresponding field patterns were also obtained. It was found that the effect of  $l$  on the radiation patterns was negligibly small.

The effects of the probe displacement  $b$  on the peak resistance and (probe-loaded) resonant frequency are shown in Fig. 10(a) and (b), respectively, for  $l = 6.5, 7.5$ , and  $8.5$  mm with  $c = 4$  mm. With reference to Fig. 10(a), the peak resistance first increases with  $b$  until it reaches a maximum value. It is found that the longer the probe length is, the higher the peak resistance. Fig. 10(b) shows that the resonant frequency decreases with increasing  $b$  and  $l$ . The results of Figs. 9 and 10 suggest that the probe length and probe displacement can be used to achieve the impedance matching.

#### IV. CONCLUSION

The probe-fed hemispherical DRA with a concentric conductor has been studied theoretically in this paper, with the

DRA excited at the broadside  $\text{TE}_{111}$  mode. The mode-matching method has been used to derive the characteristic equation of the new configuration, from which the source-free  $\text{TE}_{111}$ -mode resonant frequency and  $Q$ -factor have been found. For the engineering purpose, two simple curve-fitting formulas for the resonant frequency and  $Q$ -factor have been presented. To study the radiation characteristics of the new configuration, the exact Green's functions for evaluation of the input impedance and radiation patterns have been derived and presented in computationally efficient forms. The probe current and, hence, the input impedance, have been found using the MoM. Using the concentric conductor a wider bandwidth and a higher resonant frequency have been obtained. It has been found that the  $E$ -plane field pattern of this configuration is asymmetric, but the asymmetry can be reduced by using a higher dielectric constant. The effects of the probe length and probe displacement on the input resistance and resonant frequency have been examined. It has been found that the impedance matching can be achieved by varying the probe length and/or the probe position.

Finally, it should be mentioned that the present theory is very general and can be applied to other problems, such as to the solid DRA and to a wire antenna in the presence of a hemispherical conductor.

#### APPENDIX A

The various modal coefficients in (4b) are as follows:

$$j_n = \frac{-1}{\delta_n^{\text{TM}}} \left[ \hat{J}_n(kr') - \frac{\hat{H}_n^{(2)}(kr') \hat{J}'_n(kc)}{\hat{H}_n^{(2)}(kc)} \right] \cdot T_n^m \quad (\text{A1})$$

$$e_n = \frac{-1}{\delta_n^{\text{TM}}} \left[ \hat{J}'_n(kr') - \frac{\hat{H}_n^{(2)}(kr') \hat{J}'_n(kc)}{\hat{H}_n^{(2)}(kc)} \right] \cdot T_n^m \quad (\text{A2})$$

$$b_n = \frac{-1}{\delta_n^{\text{TE}}} \left[ \hat{J}_n(kr') - \frac{\hat{H}_n^{(2)}(kr') \hat{J}_n(kc)}{\hat{H}_n^{(2)}(kc)} \right] \cdot T_n^e \quad (\text{A3})$$

$$k_n = \frac{1}{\delta_n^{\text{TM}}} \cdot \frac{\hat{J}'_n(kc)}{\hat{H}_n^{(2)}(kc)} \cdot \left[ \hat{J}_n(kr') T_n^m - \hat{H}_n^{(2)}(kr') \Delta_n^{\text{TM}} \right] \quad (\text{A4})$$

$$c_n = \frac{1}{\delta_n^{\text{TE}}} \cdot \frac{\hat{J}_n(kc)}{\hat{H}_n^{(2)}(kc)} \cdot \left[ \hat{J}_n(kr') T_n^e - \hat{H}_n^{(2)}(kr') \Delta_n^{\text{TE}} \right] \quad (\text{A5})$$

$$f_n = \frac{1}{\delta_n^{\text{TM}}} \cdot \frac{\hat{J}'_n(kc)}{\hat{H}_n^{(2)}(kc)} \cdot \left[ \hat{J}'_n(kr') T_n^m - \hat{H}_n^{(2)}(kr') \Delta_n^{\text{TM}} \right] \quad (\text{A6})$$

$$\delta_n^{\text{TE}} = \Delta_n^{\text{TE}} - \frac{\hat{J}_n(kc)}{\hat{H}_n^{(2)}(kc)} \cdot T_n^e \quad (\text{A7})$$

$$\Delta_n^{\text{TE}} = \hat{J}_n(ka) \hat{H}_n^{(2)}(k_0 a) - \frac{k}{k_0} \hat{J}'_n(ka) \hat{H}_n^{(2)}(k_0 a) \quad (\text{A8})$$

$$T_n^e = \hat{H}_n^{(2)}(ka) \hat{H}_n^{(2)}(k_0 a) - \frac{k}{k_0} \hat{H}_n^{(2)}(ka) \hat{H}_n^{(2)}(k_0 a) \quad (\text{A9})$$

$$\delta_n^{\text{TM}} = \Delta_n^{\text{TM}} - \frac{\hat{J}'_n(kc)}{\hat{H}_n^{(2)}(kc)} \cdot T_n^m \quad (\text{A10})$$

$$\Delta_n^{\text{TM}} = \hat{J}'_n(ka) \hat{H}_n^{(2)}(k_0 a) - \frac{k}{k_0} \hat{J}_n(ka) \hat{H}_n^{(2)}(k_0 a) \quad (\text{A11})$$

$$T_n^m = \hat{H}_n^{(2)}(ka) \hat{H}_n^{(2)}(k_0 a) - \frac{k}{k_0} \hat{H}_n^{(2)}(ka) \hat{H}_n^{(2)}(k_0 a). \quad (\text{A12})$$

#### APPENDIX B

The  $\text{TE}_{1mr}$ -mode ( $m = 0, 1, 2, \dots$  and  $r = 1, 2, \dots$ ) characteristic equation of the hemispherical DRA with an air gap is given by

$$\delta_n^{\text{TE}} = 0 \quad (\text{B1})$$

where

$$\delta_n^{\text{TE}} = \left[ \hat{J}'_n(k_0 c) \hat{H}_n^{(2)}(kc) - \frac{k}{k_0} \hat{J}_n(k_0 c) \hat{H}_n^{(2)}(kc) \right] \Delta_n^{\text{TE}} - \left[ \hat{J}'_n(k_0 c) \hat{J}_n(kc) - \frac{k}{k_0} \hat{J}_n(k_0 c) \hat{J}'_n(kc) \right] T_n^e \quad (\text{B2})$$

In (B2),  $\Delta_n^{\text{TE}}$  and  $T_n^e$  are given in (A8) and (A9), respectively, and  $c$  is now the radius of the air gap.

#### ACKNOWLEDGMENT

The author would like to thank the reviewers for their valuable comments. The assistance of K. W. Chan, City University of Hong Kong, Hong Kong, in obtaining the curve-fitting formulas (13) and (14) is gratefully appreciated. The radiation patterns were generated by K. K. Tse, City University of Hong Kong, Hong Kong.

#### REFERENCES

- [1] S. A. Long, M. W. McAllister, and L. C. Shen, "The resonant cylindrical dielectric cavity antenna," *IEEE Trans. Antennas Propagat.*, vol. AP-31, pp. 406–412, May 1983.
- [2] R. A. Kranenburg and S. A. Long, "Microstrip transmission line excitation of dielectric resonator antennas," *Electron. Lett.*, vol. 24, pp. 1156–1157, 1988.
- [3] R. A. Kranenburg, S. A. Long, and J. T. Williams, "Coplanar waveguide excitation of dielectric resonator antennas," *IEEE Trans. Antennas Propagat.*, vol. 39, pp. 119–121, Jan. 1991.
- [4] J. T. S. H. Martin, Y. M. M. Antar, A. A. Kishk, A. Ittipiboon, and M. Cuhaci, "Dielectric resonator antenna using aperture coupling," *Electron. Lett.*, vol. 28, pp. 2015–2016, 1990.
- [5] R. K. Mongia, A. Ittipiboon, Y. M. M. Antar, P. Bhartia, and M. Cuhaci, "A half-split cylindrical dielectric resonator antenna using slot-coupling," *IEEE Microwave Guided Wave Lett.*, vol. 3, pp. 38–39, Jan. 1993.
- [6] K. W. Leung, K. M. Luk, K. Y. A. Lai, and D. Lin, "Theory and experiment of probe fed dielectric resonator antenna," *IEEE Trans. Antennas Propagat.*, vol. 41, pp. 1390–1398, Oct. 1993.
- [7] A. A. Kishk, G. Zhou, and A. W. Glisson, "Analysis of dielectric-resonator antennas with emphasis on hemispherical structures," *IEEE Antennas Propagat. Mag.*, vol. 36, pp. 20–31, Apr. 1994.
- [8] K. L. Wong, N. C. Chen, and H. T. Chen, "Analysis of a hemisphere dielectric resonator antenna with an airgap," *IEEE Microwave Guided Wave Lett.*, vol. 3, pp. 355–357, Oct. 1993.
- [9] K. M. Luk, K. W. Leung, and E. K. N. Yung, "Hemispherical dielectric resonator with a concentric conductor," in *IEEE AP-S Int. Symp. Dig.*, Newport Beach, CA, June 1995, pp. 730–733.
- [10] G. P. Junker, A. A. Kishk, and A. W. Glisson, "Input impedance of dielectric resonator antennas excited by a coaxial probe," *IEEE Trans. Antennas Propagat.*, vol. 42, pp. 960–966, July 1994.

- [11] S. M. Shum and K. M. Luk, "FDTD analysis of probe-fed cylindrical dielectric resonator antenna operating in fundamental broadside mode," *Electron. Lett.*, vol. 31, pp. 1210–1212, 1995.
- [12] C. M. Butler and T. L. Keshavamurthy, "Analysis of a wire antenna in the presence of sphere," *IEEE Trans. Electromagn. Compat.*, vol. EMC-22, pp. 113–118, May 1980.
- [13] K. K. Tse, K. W. Leung, K. M. Luk, and E. K. N. Yung, "Radiation from a wire antenna/hemispherical structure," in *IEEE AP-S Int. Symp. Dig.*, vol. 1, Montreal, QC, Canada, July 1997, pp. 252–255.
- [14] M. Gastine, L. Courtois, and J. Dormann, "Electromagnetic resonances of free dielectric spheres," *IEEE Trans. Microwave Theory Tech.*, vol. MTT-15, pp. 694–700, Dec. 1967.
- [15] R. F. Harrington, *Time-Harmonic Electromagnetic Fields*. New York: McGraw-Hill, 1961.
- [16] R. C. Hansen, "Formulation of echelon dipole mutual impedance for computer," *IEEE Trans. Antennas Propagat.*, vol. AP-20, pp. 780–781, Nov. 1972.
- [17] D. M. Pozar, *Antenna Design Using Personal Computers*. Norwood, MA: Artech House, 1985, pp. 35–43.
- [18] M. Abramowitz and I. A. Stegun, *Handbook of Mathematical Functions*. New York: Dover, 1970, pp. 231–233.
- [19] W. A. Imbriale and P. G. Ingerson, "On numerical convergence of moment solutions of moderately thick wire antennas using sinusoidal basis functions," *IEEE Trans. Antennas Propagat.*, vol. AP-21, pp. 363–366, May 1973.



**Kwok Wa Leung** (S'91–M'92) was born in Hong Kong, on April 11, 1967. He received the B.Sc. degree in electronics and the Ph.D. degree in electronic engineering from the Chinese University of Hong Kong, Kowloon, Hong Kong, in 1990 and 1993, respectively.

From 1990 to 1993, he was a Graduate Assistant in the Department of Electronic Engineering, Chinese University of Hong Kong. In 1994, he joined the Department of Electronic Engineering, City University of Hong Kong, Kowloon, Hong Kong, as an Assistant Professor and became an Associate Professor in 1999. His research interests include DRAs, microstrip antennas, wire antennas, numerical methods in electromagnetics, and mobile communications.